communications earth & environment

ARTICLE

https://doi.org/10.1038/s43247-023-00785-7 OPEN

Atmospheric trends explained by changes in frequency of short-term circulation patterns

Irina Rudeva[1✉], Ghyslaine Boschat[1,2], Chris Lucas[1], Linden Ashcroft[2,3], Acacia Pepler[4] & Pandora Hope[1,2]

The circulation of the atmosphere is subject to natural and anthropogenic forcings that alter the energy balance of the climate system. In each hemisphere the zonally averaged atmospheric circulation can be represented by a single overturning cell if viewed in isentropic coordinates, highlighting the connections between tropics and extratropics. Here we present clusters of the meridional atmospheric circulation based on reanalysis data. Our results reveal preferred global circulation regimes with two clusters in each solstice season. These clusters show strong trends in their occurrence in the last two decades of the 20th century coincident with the depletion of the low-stratospheric ozone over Antarctica. We hypothesize that a change in the occurrence of short-term circulation regimes may lead to some long-term atmospheric trends. Finally, we show a strong coupling between the atmospheric circulation in boreal and austral winters and propose a mechanism linking anomalies in both seasons to the stratospheric ozone that requires confirmation with modelling experiments.

[1] Australian Bureau of Meteorology, Melbourne, VIC, Australia. [2] ARC Centre of Excellence for Climate Extremes, Melbourne, VIC, Australia. [3] School of Geography, Earth and Atmospheric Sciences, University of Melbourne, Parkville, VIC, Australia. [4] Australian Bureau of Meteorology, Sydney, NSW, Australia. ✉email: irina.rudeva@bom.gov.au

In recent decades the global atmospheric circulation has been subject to robust trends[1]. Some of these trends, such as tropical expansion and poleward shifts of the tropospheric extratropical jets, have been observed in both the Northern and Southern Hemispheres (NH and SH)[2–7]. Apart from these coherent trends, there are changes that are unique for specific regions, e.g., an increase in the mean sea-level pressure (MSLP) over subtropical regions and reduction in precipitation in Mediterranean-type climates, except in North America[8–10], an amplification of the temperature trend over the Arctic and a reduction in the annual mean Arctic sea ice[11–13], a weakening of the stratospheric polar vortex in the NH with an increased frequency of sudden stratospheric warming events[14–16], and a decrease in the lower stratospheric geopotential heights over Antarctica in spring and summer[17–19]. Some of the factors responsible for these trends include greenhouse gases, aerosols, stratospheric ozone and natural variabilities in the coupled atmosphere-ocean system[17,20–24]; however, the interaction between these is complex and may be non-linear. The global atmospheric circulation, initially forced by equator-to-pole temperature gradients, acts to bring together all changes in large-scale drivers, atmospheric composition and local forcings to create a seamless transfer of energy and momentum from the equator to higher latitudes[25]. In this study, we explore patterns of the mean meridional circulation (MMC) to identify the key global signals that emerge since 1979 and discuss plausible reasons for the observed changes.

Visualization of the global, zonally averaged circulation. The atmospheric circulation is a large-scale movement of air by which the heat is transported on the surface of the Earth[26,27]. In the absence of rotation, there would be one cell spanning from the equator to the pole in each hemisphere. However, as the Earth spins, the Coriolis force deflects the flow, causing westerlies in the upper troposphere. The air moving poleward should conserve its angular momentum, meaning that the eastward flow becomes stronger until it reaches the jet stream latitude. This is where the fast-moving air breaks down into large eddies accompanied by a sinking motion towards the surface just equatorward of the jet stream, forming a subtropical ridge near 30° in each hemisphere[28]. When it reaches the surface, the air spreads equatorward and poleward. The air rising at the equator and descending in the subtropics forms the Hadley cells.

The presence of two subsidence regions—in the subtropics and over the pole—has an important consequence for the Earth's atmospheric circulation. In the Eulerian view, the mean meridional circulation has a three-cell structure: two thermally direct cells in each hemisphere—the Hadley cell, the strongest cell, and the Polar cell—and one thermally indirect cell in the mid-latitudes, called the Ferrel cell. The latter is weak, as the poleward transport of heat and moisture is predominantly due to mid-latitude eddies rather than the mean meridional circulation[29].

Complementary to this Eulerian view, there is another, Lagrangian, framework to look at the general circulation where the zonal-mean mass-weighted meridional wind is vertically integrated between dry isentropic levels, i.e., levels of equal potential temperature, θ[26,30,31]. In this mass-weighted isentropic framework, adiabatic motions within large-scale mid-latitude weather systems are predominantly along isentropic surfaces and the thermally indirect Ferrel cell is largely eradicated leading to a single-cell thermally direct atmospheric circulation in each hemisphere (Fig. 1). Subsidence in the subtropics is still taking place, but the upward mass transport by the mid-latitude isentropic circulation is in mutual agreement with the subsidence

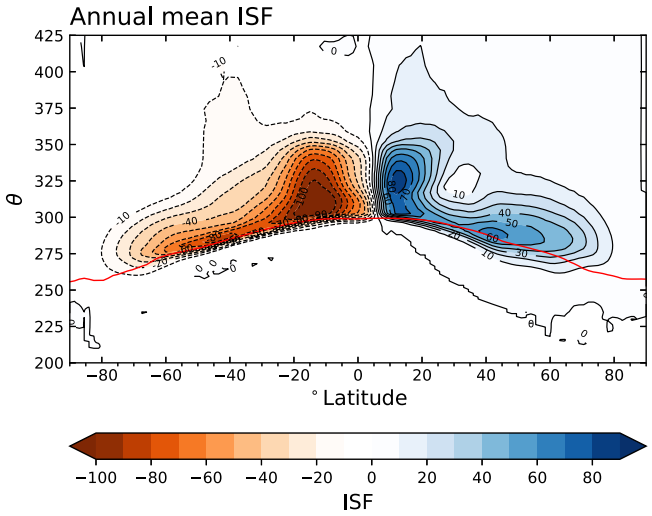

Fig. 1 Annual mean isentropic mass stream function for the period 1979–2017. The direction of the circulation is clockwise in the NH (orange) and anticlockwise in the SH (blue), represented by positive and negative dry isentropic stream function values, Ψ (10^9 kg s^{-1}), respectively. The red line shows the average median surface potential temperature.

in the downward Hadley cell branch in the subtropics[31]. As baroclinic eddies are a part of the mass-weighted isentropic MMC[30,32–34], it becomes a powerful approach in the analysis of variability and changes in the global circulation.

Sources of climate variability and change. Climate drivers are processes that act on the atmospheric and oceanic circulations by changing the Earth's energy balance either globally or locally. More specifically, large-scale drivers can modify the circulation including by changing temperature gradients and the atmospheric static stability. Anomalies, caused by climate drivers, may have a broad impact on the global atmospheric circulation via teleconnections[35–43]. In this section, we introduce the sources of climate variability and change that are key to interpreting our results.

The first climate driver that comes to mind is the greenhouse gases, that have been linked to surface warming and increased equator to pole temperature gradient in the upper tropical troposphere and lower polar stratosphere[1,44]. Another important climate driver, particularly for the atmospheric circulation in the SH, is the stratospheric ozone, which has been decreasing since the 1960s until the end of the 20th century. The reduction in the lower stratospheric ozone caused cooling of the air over the SH polar regions during austral spring, altering the equator-to-pole temperature gradient[19,45]. A few studies have linked trends in the SH troposphere, such as a positive trend in the Southern Annular mode (SAM), poleward shift in the eddy-driven jet stream and widening of the Hadley cell[17,46–49]. However, starting from around the late-1990s, the spring stratospheric ozone decline has paused leading to a pause in the SAM trend during austral summer. In contrast to the SH polar region, the Arctic has warmed faster than the global average – a process called Arctic Amplification, leading to a rapid and asymmetric decline in Arctic Sea ice, particularly, in the Barents and Kara Sea[12,50–52]. The asymmetric Arctic warming may affect the circulation in the NH mid-latitudes, leading to more frequent cold air advection[13,15,53,54].

Another source of atmospheric variability comes from the ocean. The main mode of oceanic interannual variability is ENSO, which alternates between anomalously warm (El Niño) and cool (La Niña) sea surface temperature (SST) conditions in

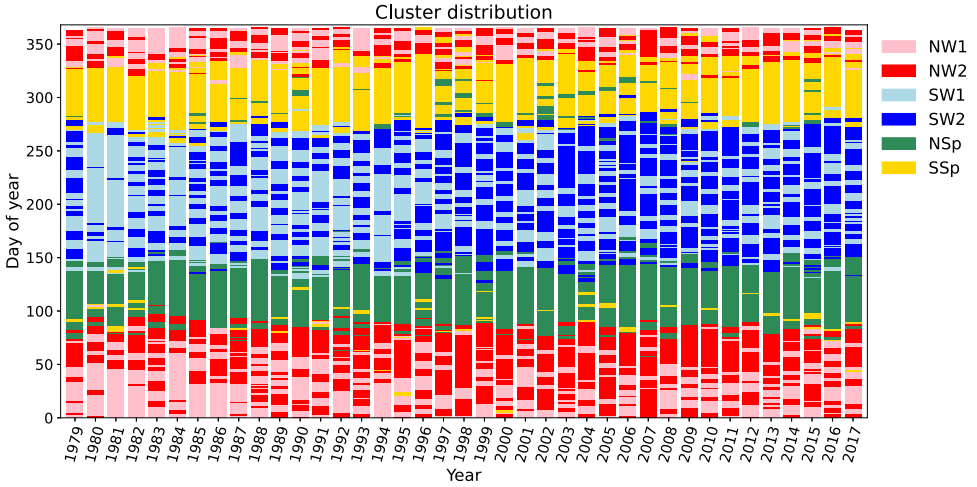

Fig. 2 Distribution of MMC cluster occurrence. Clusters are well separated by the seasons. Red and pink colors represent the boreal winter (NW_1 and NW_2, respectively), light and dark blue—the austral winter (SW_1 and SW_2), green and yellow—transition seasons (*NSp* for the boreal spring and *SSp* for the austral spring).

the tropical eastern Pacific. Through the Walker circulation, the ENSO is closely linked to the Indian Ocean Dipole, which develops during boreal summer and autumn and decays by December[55,56], and the Indian Ocean basin mode, which represents a uniform ENSO-forced warming or cooling of the Indian Ocean[57]. The center of both El Niño and La Niña SST anomalies has shifted from the Eastern Pacific (EP) to the Central Pacific (CP) since 1997/98[58,59]. This change in the ENSO behavior has been linked to low-frequency tropical variability as it concurs with a change in the Pacific Decadal Oscillation (PDO) from a warm to a cold phase. Wang et al.[60] also showed that a warmer Atlantic Ocean since the early 1990s—a result of the positive phase of Atlantic multidecadal oscillation (AMO) and the global warming trend—has induced a higher frequency of CP El Niño events.

Variability in tropical SSTs not only affects local climates but also regions of the NH and SH extratropics by changing the meridional temperature gradient and by exciting atmospheric Rossby waves[43,61]. The most well-known teleconnection patterns associated with ENSO are the Pacific-North American mode (PNA) in the NH[62] and its counterpart in the SH the Pacific-South American mode (PSA)[63,64]. Both modes are forced by the ENSO, but do not necessarily occur together due to hemispheric seasonal differences[64]. Extension of the PNA mode to Eurasia has been termed as a Tropical Northern Hemisphere mode (TNH)[65]. Carleton[66] noticed that most teleconnections, even those that appear to be dominantly extratropical by origin, interact with the ENSO. Even the main modes of extratropical variability, the Arctic Oscillation in the NH and the SAM in the SH, represented by zonally symmetric anomalies, are modulated by the ENSO[67–69].

Finally, we notice that teleconnections associated with modes of climate variability can interact with each other on various timescales. For example, the Madden–Julian oscillation (MJO)[70] an intraseasonal mode of variability in the Indo-Pacific sector, can modulate the effect of ENSO and the Indian Ocean Dipole causing seasonal anomalies in their affected areas[71,72]. Studies have shown that since 1981 the MJO residence time has decreased by 3–4 days over the Indian Ocean and increased over the Maritime Continent by 5–6 days[73]. This trend is important, because convection anomalies in the MJO area, particularly around the Maritime Continent, force Rossby waves in the extratropics via anomalous divergent wind in the upper troposphere[74–76].

While this is not a comprehensive review of modes of climate variability, it illustrates the complexity of the climate system. On top of the global warming trend observed in the last decades, numerous studies showed a few important changes in the climate system that happened in the late 1990s, seen in ENSO, PDO, AMO, SAM, as well as in the trends in the stratospheric ozone and anthropogenic aerosols. The results of this study show how the global atmospheric circulation adjusted in response to these changes.

Focus of this study. The purpose of this study is to explore if there are patterns in which the global atmospheric circulation changes during the observational period. Following Lucas et al.[31], we use the mass weighted isentropic MMC, which connects the hemispheric troposphere and lower stratosphere into a single cell in each hemisphere and accounts for the mean zonal circulation, as well as stationary and transient eddies and, thus, is particularly well suited for our analysis. The dominant circulation patterns are derived using k-means cluster analysis (see Data and Methods section for further details). We show that there is an increase in the frequency of weaker MMC in the winter hemisphere prior to the late-1990s and discuss implications and possible drivers of this change.

Results

MMC clusters and trends. The long-term annual mean mass weighted isentropic MMC is represented by a single thermally direct cell in each hemisphere with the flow rising in the deep tropics, then moving quasi-horizontally (in isentropic coordinates) to the high latitudes, where it sinks and returns to the equator at the lower levels (Fig. 1; for a more detailed description of the isentropic flow see other studies[26,31]). The highest magnitude of the isentropic stream function, ψ, is found in the tropics. In the subtropics, a part of the flow descends, bounding the Hadley cell. Subtropical descent is partially compensated by an ascent by transient eddies between 15° – 40° S. On the seasonal time scale, the intensity of the isentropic MMC is the strongest during the local winter, weakening and shifting poleward in the local summer[31].

Performing cluster analysis on standardized daily anomalies of ψ, smoothed in time by a 5-day running mean, yields clusters that are well separated by season (Fig. 2). Six clusters were chosen, named according to the time of year during which they are most

frequent (*NW* for NH winter; *SW* for SH winter; *NSp* for northern spring; *SSp* for southern spring; see Data and Methods section). As shown in Fig. 2, there are two clusters that dominate in boreal winter, NW_1 and NW_2, two in austral winter, SW_1 and SW_2, and one cluster that dominates during each transition season, *NSp* (approx. March to May) and *SSp* (approx. September to November) for the NH and SH spring, respectively.

The average length of the boreal (NW_1 and NW_2 combined) and austral (SW_1 and SW_2 combined) winter MMC seasons is 120–140 days each, while transition MMC seasons are shorter than their corresponding calendar seasons—60 days for the boreal spring, *NSp*, and 47 days for the austral spring, *SSp*. The distribution of the starting and ending dates for each MMC season is shown in Supplementary Fig. 1. The MMC boreal winter, NW_1 and NW_2, starts in late-November or December and lasts until late March or April. The MMC boreal spring, *NSp*, lasts from late March or April until late June, being close to three months in duration. The MMC austral winter, SW_1 and SW_2, begins from mid-May to the end of June and lasts until September or early October. Finally, MMC austral spring, *SSp*, usually starts in early October, lasts for about one and a half months, and ends in November or early December. In contrast to studies that suggested local changes in seasonality in response to observed and projected global warming[77,78], our results show no change in MMC seasons.

The standardized (non-standardized) Ψ anomalies from the long-term annual mean for MMC clusters are shown in Fig. 3 (Supplementary Fig. 2). As would be expected, the MMC clusters reveal the seasonal differences in the global atmospheric circulation, but also highlight other important features, particularly in the solstice seasons.

In boreal winter (Fig. 3a–c, Supplementary Fig. 2a–c), both MMC clusters, NW_1 and NW_2, feature a strong circulation in the NH; however, NW_2 is weaker than NW_1 in the upper troposphere and lower stratosphere and below the mean surface temperature, which relates to the return flow during cold air advection[79,80]. The weaker winter circulation associated with NW_2 has become more frequent in the last two decades of the 20th century with a corresponding decrease in the occurrence of the stronger cluster, NW_1 (Figs. 2, 4a). During austral winter (Fig. 3d–f), the circulation anomalies in the winter hemisphere resemble those that occur during boreal winter, except that the differences between normalized MMC circulations are not observed in the return flow. The non-standardized MMC anomalies (Supplementary Fig. 2f) show that weakening in SW_2 occurs due to a reduction of the uplift in the extratropical branch of the MMC. Consistent with the boreal winter, the occurrence of SW_1 and SW_2 has strongly changed in the last two decades of the 20th century, with SW_1(SW_2) becoming less(more) frequent (Fig. 4b). Considering this trend, the weaker extratropical uplift in SW_2 is in line with earlier findings on trends in the SH MMC[31]. The transition seasons, represented by two clusters, *NSp* and *SSp*, show stronger circulation in the extratropics during local autumn, compared to spring (Fig. 3g–i and Supplementary Fig. 2g–i). However, the anomalies from the annual mean are weak in both seasons, which explains why *NSp* and *SSp* are sometimes mixed in Fig. 2. Finally, we note that results of this analysis are supported by an EOF analysis performed on the isentropic stream function,

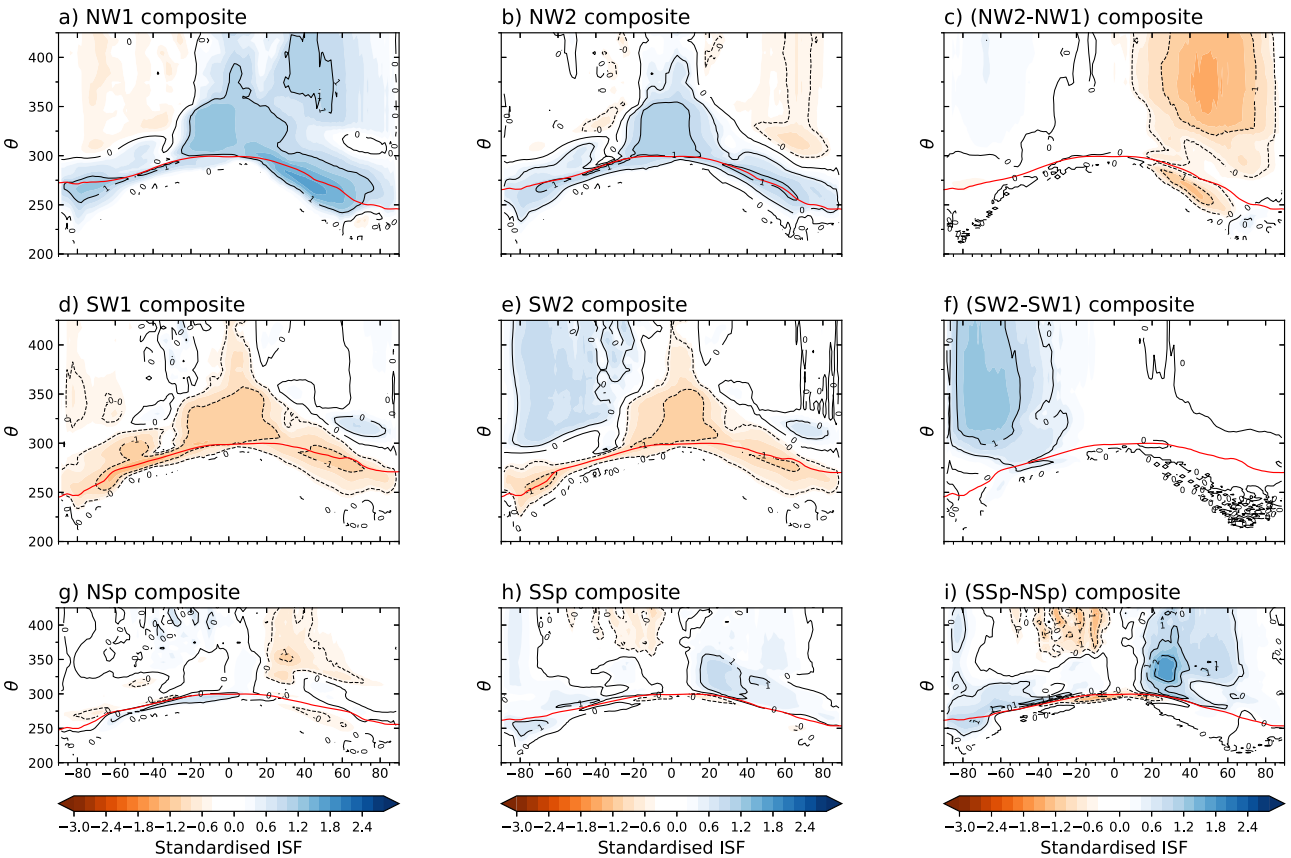

Fig. 3 Composites of the standardized isentropic stream function for each cluster. a, **b**, **d**–**h** Composite anomalies of the standardized stream function for six clusters from the annual mean. Red lines represent the location of the median surface potential temperature in shown clusters **c**, **f**, **i** The difference between clusters: (**c**) NW_1-NW_2, (**f**) SW_1-SW_2, (**i**) *SSp*-*NSp*. Colors as in Fig. 1. Red lines in (**c**, **f**, **i**) are shown for clusters NW_1, SW_1, *NSp*, respectively.

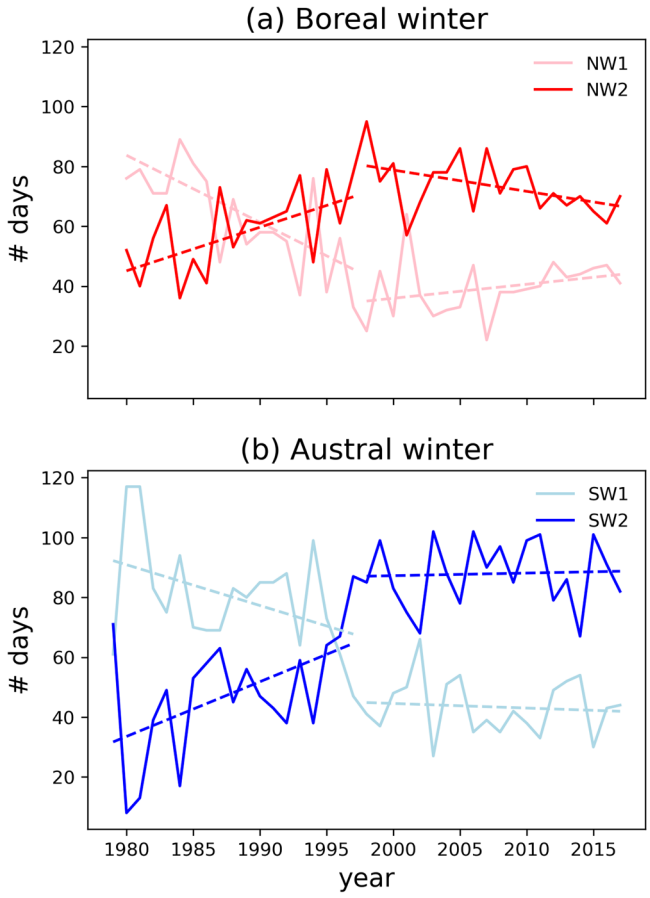

Fig. 4 Trends in cluster occurrence. (solid lines) Cluster occurrences for (**a**, pink and red) NW_1 and NW_2 and (**b**, dark and light blue) SW_1 and SW_2 in each year (days). NW_1 and NW_2 occurrences in November and December are counted in the next year. Dashed lines show linear trends for periods prior to 1998 and post 1999.

with the first two leading modes showing similar spatial patterns as Fig. 3c, f (compare with Supplementary Fig. 3a, b).

To understand the importance of the observed trends in MMC cluster frequencies, we show below that some long-term trends in the extratropics, such as the positive SAM trend, are consistent with changes implied by altered frequency of the preferred circulation regimes. For each cluster we calculated composite anomalies of selected atmospheric variables from the annual mean (Supplementary Fig. 4–9). These composites, to the first order, show seasonal anomalies, that would be expected from the distribution of cluster occurrence, such as cooler (warmer) continents in winter (summer) or a displaced ITCZ to the summer hemisphere (compare NW_1 and NW_2 with SW_1 and SW2 in Supplementary Fig. 8, 9). Furthermore, during local winter the MSLP is higher over cold continents and in the subtropics (Supplementary Fig. 4). The latter occurs due to winter intensification of the Hadley cell that leads to an intensification of the subsidence in its downward branch andstrengthening of the subtropical jet. Despite similarities between clusters within one season, our composite analysis reveals important regional differences between them, which would be difficult to deduce from the stream function anomalies shown in Fig. 3 and Supplementary Fig. 2. As the focus of this study is on the trends in the cluster occurrence in solstice seasons, we will limit our further discussion to those two seasons. We note here that, by construction, composites are not subject to long-term trends, as they are based on anomalies from the corresponding single-year annual mean (see Data and Methods for details).

Boreal winter. During boreal MMC winter (from November–December until March–early April), the MSLP composite shows a wave-like pattern in the NH with higher pressure over the Aleutian Low, north-east North America and Greenland and lower MSLP over the Far East and North America in NW_2–NW_1 composite (Fig. 5a). An increasing frequency of NW_2 during the last 20 years of the 20th century is in line with a pronounced weakening of the Siberian high[81] and increasing pressure over north-east North America. Conversely, the Aleutian Low was strong at the end of the 20th century and showed weakening signs only in the 21st century[82]. However, Smith et al.[83] suggested that the transition to a negative PDO phase that occurred in late 1990s could have been promoted by a weakening of the Aleutian Low due to aerosol forcing from Asia. Considering the intimate relationship between the Aleutian Low and the PDO[84], with trends in the Aleutian Low leading those in the PDO[82], and a reduction in the cyclone activity over the North Pacific prior to 1999[85], the trend in NW_2 supports a weakening of the Aleutian Low in the 1990s.

Figure 5c shows a Z300 composite with wave-like anomalies in the NH that resemble a Z500 regression on the correlation coefficients between the ENSO and the TNH mode (Fig. 5 in Soulard et al.[65]). Over the Pacific Ocean and North America, the TNH mode resembles an eastward shifted PNA mode, forced by EP El Niño. Unlike the PNA, the TNH also shows geopotential height anomalies over Eurasia, however, these do not match the pattern in Fig. 5c possibly due to a strong Z300 anomaly over the Sea of Japan, which may modify the wave train upstream.

In line with differences in MSLP and Z300 composites, the jet streams are shifted poleward in the North Pacific and southward in the North Atlantic in NW_2 relative to NW_1 (Fig. 6a, c). A negative NAO trend, that indicates an equatorward shift in the jet, was observed starting from 1989–2013[86,87]; at the same, in the North Pacific no long-term trend in the jet position has been found[88,89]. However, it was shown that between cool seasons of 1997/1998 and 1998/1999—strong El Niño and La Niña events, respectively—the frequency of a poleward shifted Pacific jet increased by a factor of seven[89]. Furthermore, Soulard et al.[65] suggested that the negative AMO favors a strengthened North Pacific jet that is displaced equatorward. In the 1990s and early 2000s, the AMO showed a positive trend, displacing the North Pacific jet to the north, as seen in the NW_2–NW_1 composite (Fig. 6c).

NH anomalies in the near surface air temperature (SAT) and precipitation (Fig. 7a, c) can be explained, to a large extent, by anomalous atmospheric circulation at the surface. (We remind the reader the composites are not affected by long-term trends.) Composite SAT anomalies show warmer NH continents in NW_2 in the areas of negative MSLP anomalies, and slightly reduced precipitation associated with higher MSLP in the north-east Pacific and increased rainfall in the central North Atlantic linked to lower MSLP. As long-term trends have been removed from the composites, this result suggests that dynamical changes in the global circulation may have contributed to cooling of the Arctic in NW_2; however, Arctic amplification of global warming obscured this signal in observations.

The circulation anomalies in the NH, particularly in the Pacific-North American sector, are often related to forcing from the tropical oceans. Indeed, SAT and precipitation anomalies over the tropical Pacific suggest EP El Niño conditions with a wetter and warmer Eastern Pacific and a drier Maritime Continent in the NW_2–NW_1 composite (Fig. 7a, c). Drier conditions over the

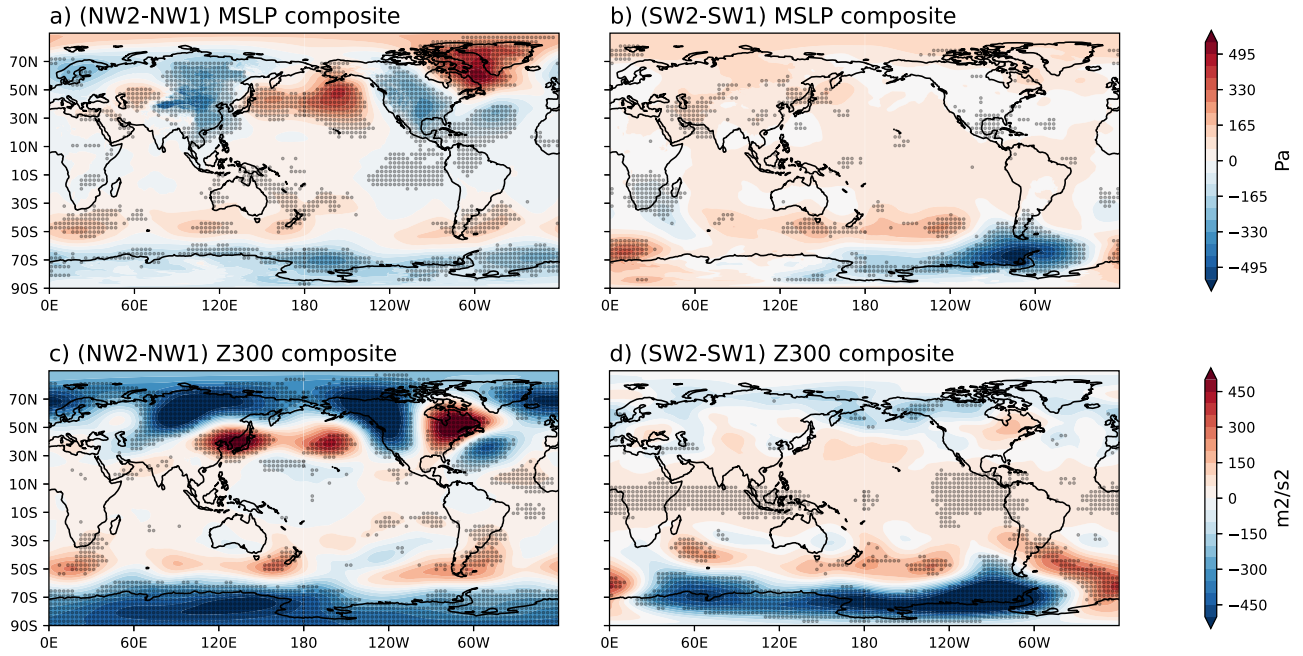

Fig. 5 MSLP and Z300 composites. Composite (**a**, **b**) MSLP (Pa) and (**c**, **d**) Z300 ($m^2\ s^{-2}$) difference between clusters in (**a**, **c**) boreal winter, NW_2–NW_1, and (**b**, **d**) austral winter, SW_2–SW_1. Stippling shows differences significant at 95% level.

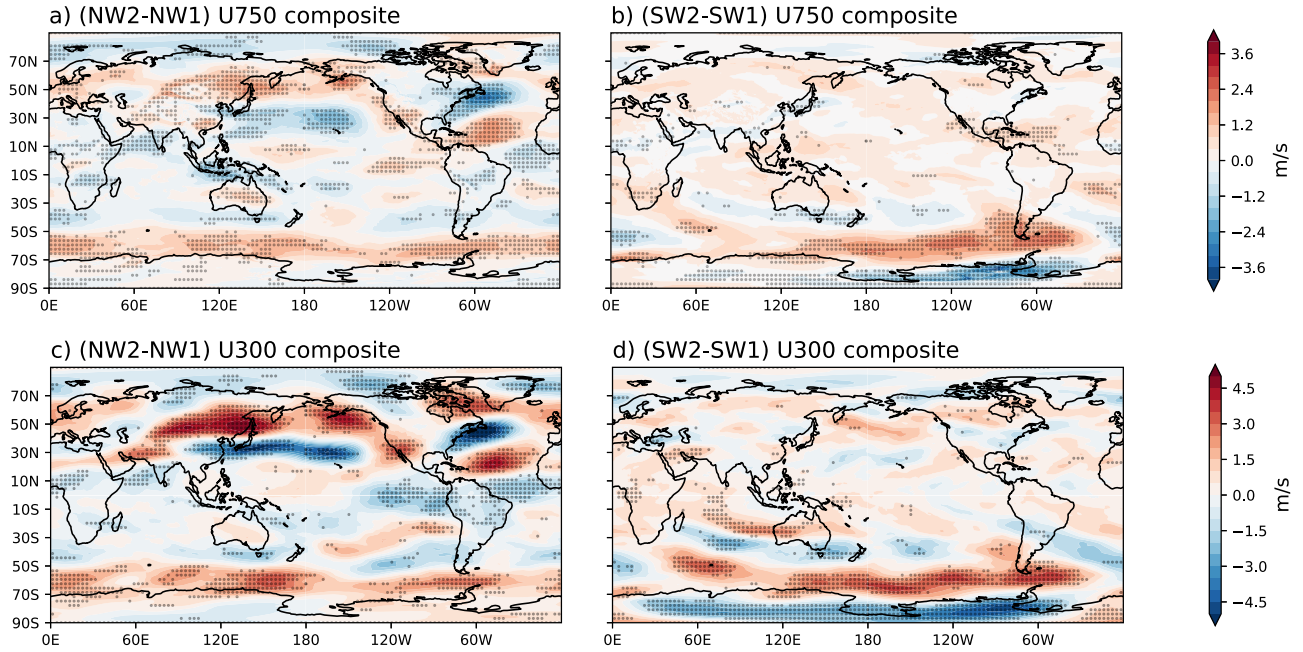

Fig. 6 U750 and U300 composites. As in Fig. 5 but for (**a**, **b**) U750 and (**c**, **d**) U300 ($m\ s^{-1}$).

western Pacific may be responsible for a strong Z300 anomaly over the Sea of Japan (Fig. 5c) due to advection of the vorticity by the divergent wind from the Maritime Continent[90]. However, in contrast to the extratropical circulation, the tropical anomalies in the NW_2–NW_1 composite do not align with changes in low-frequency modes of variability, such as PDO and AMO, and a shift to the CP El Niño events, that happened in 1990s–early 2000s. Hence, our hypothesis about trends as a change in frequency of the preferred circulation states is not supported by Fig. 7 within the tropics. Nevertheless, following the study by Roxy et al.[73], we analyzed seasonal trends in the MJO and found that there is a tendency for a longer duration of anomalous convection in the Pacific associated with the MJO, especially during boreal winter in 1990s and early 2000s (Supplementary Fig. 10).

In the SH, the MSLP composite shows a positive SAM phase with higher MSLP over subtropical continents and low mid-latitudes and lower MSLP over the Antarctic coastline in NW_2–NW_1 (Fig. 5a). The Z300 composite (Fig. 5c) also reveals a SAM-like pattern with stronger anomalies in high latitudes and, consistent with MSLP and Z300 anomalies, jets are shifted poleward in NW_2 in the lower and upper troposphere (Fig. 6a, c). This result is in agreement with a positive trend in SAM and a poleward shift of the jet during austral summer in the late 20th century[49]. The SAM was found to be negatively correlated with station-based temperature along the Antarctic coastline except for

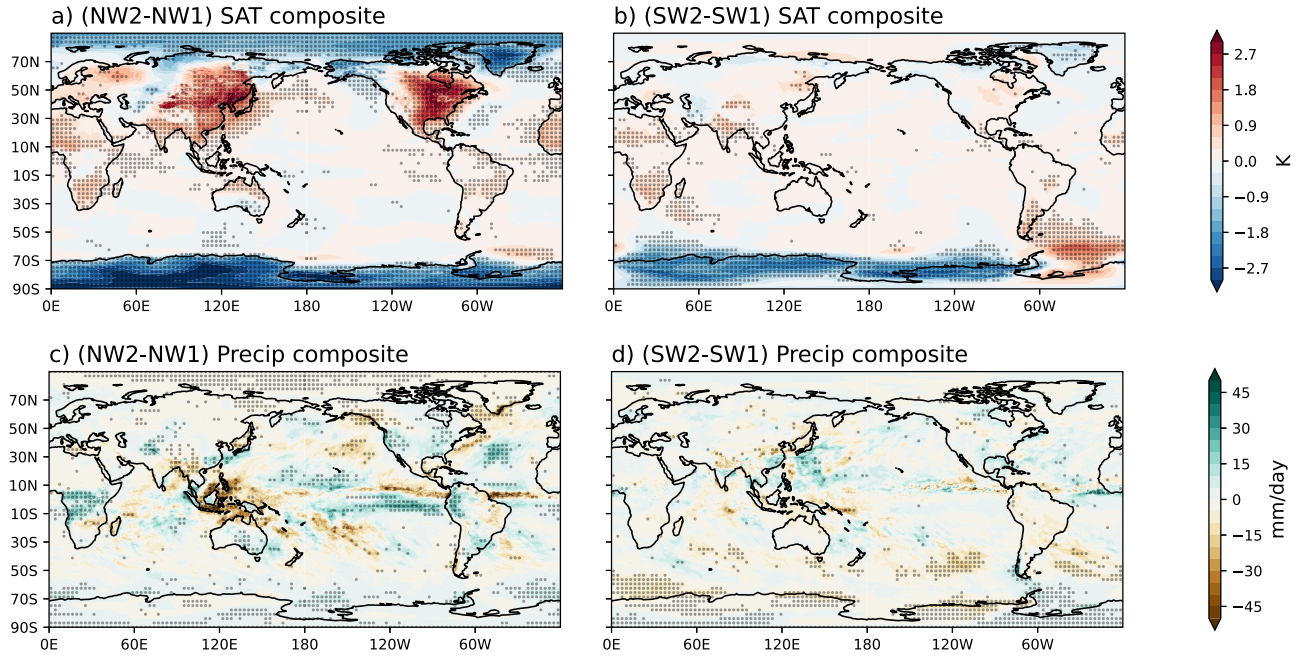

Fig. 7 Surface air temperature and precipitation composites. As in Fig. 5 but for (**a**, **b**) SAT (°C) and (**c**, **d**) precipitation (mm day^{-1}).

the Antarctic Peninsula[91]; this may explain lower temperatures over Antarctica in the NW_2–NW_1 SAT composite (Fig. 7a). From the MMC cluster analysis, the positive SAM trend during austral summer is the main change in the SH, which agrees with an earlier study showing that natural variability in the extratropical SH overwhelms the forced response in the observations except for the positive trend in the SAM[92].

Austral winter. In contrast to the boreal winter that showed coherent changes in the NH and SH hemispheres, during the MMC austral winter, differences between the two clusters, SW_2–SW_1, are limited to the winter hemisphere. Hence, the following discussion will focus on the SH.

The MSLP differences show a strong anomaly in the southern Pacific and Atlantic oceans (Fig. 5b). In SW_2, there is a strong low-pressure anomaly centered over the Drake Passage that extends to West Antarctica and a high-pressure anomaly in the southern Atlantic. A belt of high-pressure anomaly stretches in low mid-latitudes from the Indian Ocean into the Pacific. Hence, the MSLP pattern in the Indo-Pacific sector resembles a positive regional SAM; but the pattern reverses in the Atlantic sector in accord with earlier studies showing strong asymmetries in the zonal circulation during austral winter[93,94]. The atmospheric circulation in the South Pacific and Atlantic is subject to a wave train propagating from the tropical Pacific, often referred to as the PSA mode[42,95]; hence, the cyclonic and anticyclonic anomalies to the south of South America may be linked to tropical-extratropical interactions. The Z300 composite anomalies resemble those at the surface level (Fig. 6b, d) and the zonal wind in SW_2 is consistently enhanced around the Antarctic coastline throughout the troposphere (Fig. 6b, d).

In line with these circulation anomalies, the main SAT differences between clusters lie in the high latitudes of the SH (Fig. 7b). SW_2 features lower temperatures along the coastline of Antarctica except in the Weddell Sea due to the low MSLP anomaly over the Drake Passage. This cyclonic anomaly advects warm air over the Weddell Sea and brings it further inland warming the South pole, that has warmed three times faster than the global average[96]. On the other hand, lower SAT around Antarctica can be explained by the lower SST in the high latitude Southern Ocean. Surface ocean cooling around Antarctica has been linked to enhanced northward Ekman drift in response to the amplified summer polar jet that induces negative summertime SST anomalies around Antarctica, earlier sea ice freeze-up the following winter and cooler SSTs throughout the year on a short-time scale[97]. Precipitation differences between clusters in austral winter are also small and mostly not statistically significant, except for the extratropical SH, where precipitation is reduced equatorward and poleward of the polar jet but increased over the Weddell Sea following the northern flow around the MSLP anomaly (Fig. 7d).

Discussion

Understanding the mechanisms causing the weakening of the winter MMC in both hemispheres during the late 20th century warrants further analysis. It is well-established that the depletion of low stratospheric ozone in the second half of the 20th century, together with global warming, have caused a poleward shift of the SH mid-latitude circulation during austral summer[17,48,49,98]. Banerjee et al.[19] noticed that the trend in the summer jet location paused around the year 2000, in line with the ozone changes. As shown in Fig. 4, the trends in the global MMC circulation are also in agreement with the trend in the Antarctic ozone during austral spring. Furthermore, we find that the frequencies of strong and weak MMC clusters in consecutive solstice seasons are highly correlated (see Fig. 8 that shows lagged correlations between the detrended cluster frequency in the boreal winter, NW_1 (NW_2), and the following austral winter, SW_1 (SW_2). The correlation peaks from mid-1990s–2010).

Recently, Hartmann[99] proposed a mechanism linking the Antarctic stratospheric ozone to anomalies in the tropical Pacific, whereby the onset of the ozone hole since 1979 can lead to an intensification of the polar vortex and the tropospheric jet during austral spring. The latter induces an anomalous surface wind stress that causes a cooling of Southern Ocean SSTs, particularly in the South-Eastern (SE) Pacific[100]. Using a slab ocean model, Dong et al.[100] showed that tropical Pacific SSTs can be modified by cooling imposed on the SE Pacific surface heat flux. Once the tropical Pacific SST is perturbed, it drives remote changes to atmospheric circulation in the extratropics that further enhance

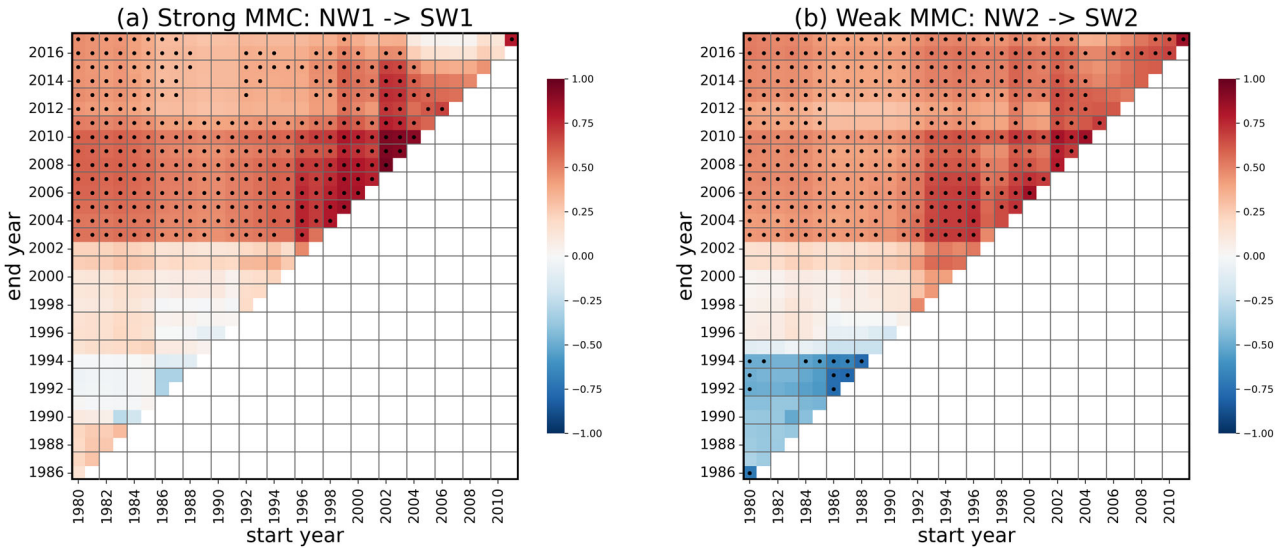

Fig. 8 Lagged correlations between cluster frequency in boreal and austral winters. Time-varying correlations between detrended timeseries of cluster occurrence during a boreal winter and the following austral winter for (**a**) NW_1 and SW_1, and (**b**) NW_2 and SW_2. The start of the time interval is indicated by the *X*-axis and the end year by the *Y*-axis. Gray dots show values significant at 90 % level.

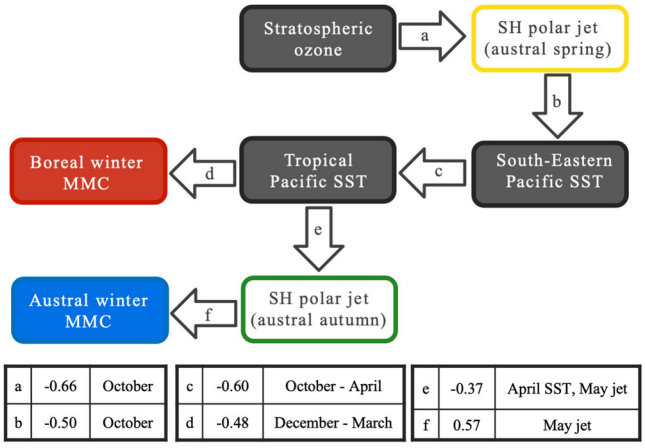

a	-0.66	October	c	-0.60	October - April	e	-0.37	April SST, May jet
b	-0.50	October	d	-0.48	December - March	f	0.57	May jet

Fig. 9 Propagation of anomalies in atmospheric and ocean circulation from austral spring to austral winter. Relationships (**a**–**f**) are supported by correlations shown in Supplementary Fig. S12. Averaged correlation coefficients for selected months across different time periods are given in the table. Stratospheric ozone is represented by the ozone mixing ratio at 100 hPa at 60–90°S, the SH polar jet by zonal mean zonal wind speed between 55–65°S, South-Eastern and Tropical Pacific SSTs are averaged across (47–62°S, 140–70°W) and (5°N–5°S, 170–120°W), respectively. Frequency of NW_2 and SW_2 are used for boreal and austral winter MMCs.

cooling in both the Southern Ocean and the tropical Pacific. Based on those findings, Hartmann[99] proposed that high-latitude surface wind anomalies associated with the Antarctic ozone hole can cause cooler temperatures over the Southern Ocean that extend into the tropics.

Based on the MMC trends (Fig. 4) and the close relationship in the strength of winter MMCs between consecutive boreal and austral winters (Fig. 8), we further hypothesize that (1) the Antarctic ozone hole can affect not only the SH, but also the NH circulation during boreal winter; (2) MMC trends in both solstice seasons may be related to the Antarctic stratospheric ozone. Validating these hypotheses requires specific modeling experiments and will form the basis of future work. Here we explore possible mechanisms based on correlation analysis using the ERA5 dataset summarized in Fig. 9. In agreement with earlier studies[17,48,49,98], we find strong correlations between the stratospheric ozone, tropospheric jet and SST variability in the SE and tropical Pacific during austral spring (Fig. 9a–c). Additional analysis shows that SST anomalies in the South-Eastern Pacific are closely linked to the anomalies of the same sign in the Niño3.4 region and SST anomalies around the Maritime Continent of the reverse sign (Supplementary Fig. 11). The latter anomalies, while smaller in amplitude, show an increasing trend in the late 20th century and pause after the year 2000. We also find a close relationship between the NW_2 frequency and the tropical SST in the Niño3.4 region (Fig. 9d) and around the Maritime Continent, supporting our hypothesis that the Antarctic ozone hole is driving global changes in the atmospheric circulation during boreal winter. A strong coupling between tropical and extratropical South Pacific persists through the boreal winter into spring (Fig. 9c). We hypothesize that tropical SST anomalies alter the intensity of the SH polar jet in the late austral autumn (Fig. 8d), and anomalies in the jet, in their turn, impact the SW_2 frequency (Fig. 9f), possibly through the eddy feedback on the mean flow[101]. Though we cannot eliminate the role of global warming and tropical variability (independent of the stratospheric ozone), we speculate here that both solstice seasons respond to anomalous SSTs in the tropical Pacific that have been modified by the Antarctic ozone since the late 20th century[17,19,45–48,100]. We emphasize here that our hypothesis is based on statistical analysis over the limited observational record and that further model experiments are needed to prove causality in these relationships. However, we should also note that a comparison of SST trends in the observational and CMIP5/6 data reveals that models fail to represent the observed SST trends in the South Pacific[102]. Considering that there is a less than 5% chance that the observed trend is due to the internal variability, model biases in the extratropical Pacific region raise a concern of whether relationships shown in Fig. 9 can be skillfully represented in the current generation of climate models.

Finally, there is an apparent disagreement between the weakening of the SH MMC (Fig. 3c and Supplementary Fig. 2c) and an intensification of the winter mid-latitude storm track (at 50°S) since around 1980, revealed by the increasing eddy moist static

energy flux[103]. A similar inconsistency has been shown for positive phases of the SAM that lead to an increased poleward flux of the eddy moist static energy in combination with even stronger increase in the equatorward flux of the dry static energy by the steady flow[104]. Therefore, the weakening of the dry isentropic SH MMC found in this study should not be interpreted as a weakening of the winter storm track but, instead, suggests its strengthening (Fig. 6b, d).

Conclusions

This work explores variability in the global atmospheric circulation by identifying preferred regimes in the 5-day smoothed isentropic MMC. The motivation behind this work was to investigate how transient regimes integrate into long-term atmospheric trends. In contrast to the isobaric MMC, the circulation in the isentropic framework accounts for (some) energy transport by extratropical eddies, forming a single direct cell in each hemisphere. Therefore, changes in the MMC represent a cumulative effect of forcings in different parts of the globe. In light of multiple changes in a range of climate drivers, from tropical SST to stratospheric ozone, the isentropic framework is particularly well suited for an analysis of atmospheric response to those changes.

This study is based on six k-means clusters defined using smoothed daily MMC data. These clusters reflect four main seasons with two clusters allocated to each solstice season and one cluster to each transition season. We found decreasing trends in the frequency of clusters that show stronger MMC circulation and an increasing frequency of weaker MMC circulation in the winter hemisphere, with a change occurring around 1998. These trends have happened alongside a number of changes in climate drivers, e.g., a decreasing trend in the lower stratospheric temperature in high SH latitudes that paused after the late 1990s, a transition to a negative PDO that lagged an earlier transition of the AMO to a warm phase. While our analysis does not prove causality, it does show that the atmospheric circulation adapted to those shifts in climate drivers, with the NH and SH experiencing many coherent changes. Moreover, our results demonstrate that long-term trends in the atmospheric circulation, e.g., a positive SAM and negative NAO trend, weakening of the Siberian High, strengthening of high pressure over Greenland, can be a cumulative effect of changes in the frequency of preferred short-term global circulation regimes.

We note here that the analysis of recent changes in the MMC explains very broad tendencies in the atmospheric circulation that can be still modified by other modes of variability (e.g., Supplementary Fig. 3c). An important finding from this work is that the large-scale atmospheric circulation has a number of preferred states, and some long-term trends are made up by a change in frequencies of those synoptic states.

Data and methods

Dry isentropic circulation and clusters. The dry isentropic MMC was calculated by Lucas et al.[31] using the European Centre for Medium-Range Weather Forecasts (ECMWF) Interim Reanalysis (ERA-Interim) for the period 1979–2017[105] on 60 model levels from the surface to ~1 hPa with the horizontal resolution 1.5° × 1.5°. Calculations were based on meridional wind and temperature at 12 UTC. The 29th of February was removed from the analysis.

The ERA-Interim data were interpolated onto isentropic levels between 210 K and 450 K, covering the full range of potential temperature θ within the troposphere from tropics to high latitudes and extending into the lower stratosphere in polar regions. The dry isentropic stream function Ψ is defined by:

$$\Psi = -2\pi a \cos\phi \int_{\theta_b}^{\theta} \bar{v}\bar{\rho}_\theta \mathrm{d}\theta, \quad (1)$$

where overbar denotes zonal mean, a is the equatorial radius of the Earth, ϕ is the latitude, v is the instantaneous meridional wind, ρ_θ is the isentropic density ($\rho_\theta = -\frac{1}{g}\frac{\partial p}{\partial \theta}$), and θ_b is the potential temperature at the surface. The resulting isentropic stream function was smoothed with a 5-day average.

The circulation patterns in the MMC are categorized using k-means cluster analysis, applied to smoothed MMC fields for each day of the year. We emphasize here that no season was selected a priori. Before clustering, the stream function values at each grid point Ψ_i were standardized by subtracting the long-term mean $\Psi_{i,\mathrm{mean}}$ and dividing by the standard deviation σ_i: $\Psi_{i,s} = \frac{\Psi_i - \Psi_{i,\mathrm{mean}}}{\sigma_i}$. The last step is important as clustering is based on the Euclidean distance, which emphasizes changes in the low-latitude troposphere, where Ψ is the largest (Fig. 1), should the raw Ψ be used. Without standardization, the clusters are not well defined; however, after standardisation high-level anomalies start playing a more significant role in forming the circulation patterns shown in Fig. 3. We preselected six MMC clusters as they automatically separated by seasons (Fig. 2). Occasionally, clusters may be seen in a different season, which happens more often during transition periods. Consistent with this, if the number of clusters is reduced from six to five, both transition seasons form one cluster, while solstice seasons remain almost unchanged being represented by two clusters each.

The correlation between the timeseries of cluster occurrences in Fig. 8 is calculated using the Pearson correlation coefficient, the statistical significance based on a t-test.

Atmospheric variables and their composites. Analysis of atmospheric fields associated with the MMC clusters was made using a more recent ECMWF Reanalysis v5 (ERA5)[106], which replaced the ERA-Interim. The new dataset benefited from improved model physics, core dynamics and data assimilation. It has also higher temporal and spatial resolution, which should have improved the model dynamics. For Figs. 5–7 and S3–S8 we use the mean sea-level pressure (MSLP), zonal wind speed at 300 and 750 hPa (U300 and U750), geopotential height of 300 hPa (Z300), near surface air temperature at 2 m (SAT), and total precipitation rate at 0.25° horizontal resolution. All but one variable are derived every 6 h and then averaged daily. Precipitation is integrated daily using hourly total precipitation rates. For Fig. 9 and Supplementary Fig. 12, we use monthly mean ERA5 datasets.

For each cluster C, we calculated composite anomalies of an atmospheric variable V from the annual mean as:

$$V'_{C,yr} = \frac{1}{n}\sum_{i=1}^{n} \hat{V}_{i,C,yr} - \bar{V}_{yr}, \quad (2)$$

where i is a single occurrence of cluster C in year yr (Fig. 2), n is the number of days attributed to cluster C in yr, $\hat{V}$ indicates anomaly from the climatological seasonal cycle and V'_{yr} is the single-year annual mean of V. Some variables, e.g., SAT and MSLP, are strongly affected by the seasonal cycle even within one season. Hence, daily anomalies due to the mean seasonal cycle are calculated as wave 1 in climatological daily means using the Fast Fourier transform and removed from V. The single year annual mean, $\bar{V}_{yr}$, is subtracted to reduce the effect of global warming and other long-term trends on $V'_{C,yr}$.

The long-term mean cluster anomaly, $\langle V'_C \rangle$, is derived as $V'_{C,yr}$ averaged across all years in 1979–2017. As some clusters are

becoming more or less frequent over the years, we first calculate the annual anomaly $V'_{C,yr}$ and then average across all years so that each year contributes equally. The difference in composite values (Figs. 5–7) is tested by the Kolmogorov–Smirnov test. To test the robustness of our results we also performed composites using ERA-Interim and found very similar patterns.

Data availability

The MMC data used for clustering can be found at https://figshare.com/articles/dataset/daily_ISF/22116602. ERA5 data on single and pressure levels were downloaded from the Copernicus Climate Data Store (https://doi.org/10.24381/cds.adbb2d47 and https://doi.org/10.24381/cds.bd0915c6, respectively).

Code availability

Code is available upon request to the corresponding author.

Received: 17 May 2022; Accepted: 30 March 2023;
Published online: 19 April 2023

References

1. Gulev, S. K. et al. Changing State of the Climate System. In *Climate Change 2021: The Physical Science Basis. Contribution of Working Group I to the Sixth Assessment Report of the Intergovernmental Panel on Climate Change.* (eds Masson-Delmotte, V. et al.) pp. 287–422, https://doi.org/10.1017/9781009157896.004 (Cambridge University Press, Cambridge, United Kingdom and New York, NY, USA, 2021).
2. Seidel, D. J., Fu, Q., Randel, W. J. & Reichler, T. J. Widening of the tropical belt in a changing climate. *Nat. Geosci.* **1**, 21–24 (2008).
3. Archer, C. L. & Caldeira, K. Historical trends in the jet streams. *Geophys. Res. Lett.* **35**, (2008).
4. Kang, S. M. & Polvani, L. M. The interannual relationship between the latitude of the eddy-driven jet and the edge of the Hadley cell. *J. Clim.* **24**, 563–568 (2011).
5. Lucas, C., Nguyen, H. & Timbal, B. An observational analysis of Southern Hemisphere tropical expansion. *J. Geophys. Res. Atmos.* **117**, (2012).
6. Lucas, C., Timbal, B. & Nguyen, H. The expanding tropics: a critical assessment of the observational and modeling studies. *WIREs Clim. Change* **5**, 89–112 (2014).
7. Lucas, C. & Nguyen, H. Regional characteristics of tropical expansion and the role of climate variability. *J. Geophys. Res. Atmos.* **120**, (2015).
8. Cai, W., Cowan, T. & Thatcher, M. Rainfall reductions over Southern Hemisphere semi-arid regions: the role of subtropical dry zone expansion. *Sci. Rep.* **2**, 702 (2012).
9. Schmidt, D. F. & Grise, K. M. The Response of Local Precipitation and Sea Level Pressure to Hadley Cell Expansion. *Geophys. Res. Lett.* **44**, 10,573–10,582 (2017).
10. Seager, R. et al. Climate variability and change of mediterranean-type climates. *J. Clim.* **32**, 2887–2915 (2019).
11. Swart, N. C., Fyfe, J. C., Hawkins, E., Kay, J. E. & Jahn, A. Influence of internal variability on Arctic sea-ice trends. *Nat. Clim. Change* **5**, www.nature.com/natureclimatechange (2015).
12. Cohen, J. et al. Recent Arctic amplification and extreme mid-latitude weather. *Nat. Geosci.* **7**, 627–637 (2014).
13. Cohen, J. et al. Divergent consensuses on Arctic amplification influence on midlatitude severe winter weather. *Nat. Clim. Change* **10**, 20–29 (2020).
14. Reichler, T., Kim, J., Manzini, E. & Kröger, J. A stratospheric connection to Atlantic climate variability. *Nat. Geosci.* **5**, 783–787 (2012).
15. Zhang, J., Tian, W., Chipperfield, M. P., Xie, F. & Huang, J. Persistent shift of the Arctic polar vortex towards the Eurasian continent in recent decades. *Nat. Clim. Chang.* **6**, 1094–1099 (2016).
16. Seviour, W. J. M. Weakening and shift of the Arctic stratospheric polar vortex: Internal variability or forced response? *Geophys. Res. Lett.* **44**, 3365–3373 (2017).
17. Polvani, L. M., Waugh, D. W., Correa, G. J. P. & Son, S. W. Stratospheric ozone depletion: the main driver of twentieth-century atmospheric circulation changes in the Southern Hemisphere. *J. Clim.* **24**, 795–812 (2011).
18. Kidston, J. et al. Stratospheric influence on tropospheric jet streams, storm tracks and surface weather. *Nat. Geosci.* **8**, 433–440 (2015).
19. Banerjee, A., Fyfe, J. C., Polvani, L. M., Waugh, D. & Chang, K. L. A pause in Southern Hemisphere circulation trends due to the Montreal Protocol. *Nature* **579**, 544–548 (2020).
20. Thompson, D. W. J. & Solomon, S. Interpretation of recent Southern Hemisphere climate change. *Science* **296**, 895–899 (2002).
21. Gillett, N. P., Fyfe, J. C. & Parker, D. E. Attribution of observed sea level pressure trends to greenhouse gas, aerosol, and ozone changes. *Geophys. Res. Lett.* **40**, 2302–2306 (2013).
22. Allen, R. J., Norris, J. R. & Kovilakam, M. Influence of anthropogenic aerosols and the Pacific Decadal Oscillation on tropical belt width. *Nat. Geosci.* **7**, 270–274 (2014).
23. Garfinkel, C. I., Waugh, D. W. & Polvani, L. M. Recent Hadley cell expansion: the role of internal atmospheric variability in reconciling modeled and observed trends. *Geophys. Res. Lett.* **42**, 10824–10831 (2015).
24. Nguyen, H., Lucas, C., Evans, A., Timbal, B. & Hanson, L. Expansion of the Southern Hemisphere hadley cell in response to greenhouse gas forcing. *J. Clim.* **28**, 8067–8077 (2015).
25. Trenberth, K. E. & Stepaniak, D. P. Covariability of components of poleward atmospheric energy transports on seasonal and interannual timescales. *J. Clim.* **16**, 3691–3705 (2003).
26. Schneider, T. The general circulation of the atmosphere. *Annu. Rev. Earth Planet. Sci.* **34**, 655–688 (2006).
27. Catling, D. C. in *Treatise on Geophysics* Vol. 10, 2nd edn, (ed. Schubert, G.) 429–472 (Elsevier Inc., 2015).
28. Held, I. M. The general circulation of the atmosphere. 2000 WHOI GFD Program, Woods Hole Oceanographic Institution, Woods Hole, MA, p 54. (2000).
29. Lu, J. & Vecchi, G. A. in *Encyclopedia of Atmospheric Sciences* Vol. 6, (eds North, G. R., Pyle, J. A. & Zhang, F.) 113–120 (Elsevier, 2015).
30. Townsend, R. D. & Johnson, D. R. A diagnostic study of the isentropic zonally averaged mass circulation during the first GARP global experiment. *J. Atmos. Sci.* **42**, 1565–1579 (1985).
31. Lucas, C., Rudeva, I., Nguyen, H., Boschat, G. & Hope, P. Variability and changes to the mean meridional circulation in isentropic coordinates. *Clim. Dyn.* **58**, 257–276 (2022).
32. Pauluis, O., Czaja, A. & Korty, R. The global atmospheric circulation on moist isentropes. *Science* **321**, 1075–1078 (2008).
33. Pauluis, O., Czaja, A. & Korty, R. The global atmospheric circulation in moist isentropic coordinates. *J. Clim.* **23**, 3077–3093 (2010).
34. Yamada, R. & Pauluis, O. Momentum balance and Eliassen–Palm flux on moist isentropic surfaces. *J. Atmos. Sci.* **73**, 1293–1314 (2016).
35. Lau, N.-C. Interactions between global SST anomalies and the midlatitude atmospheric circulation. *Bull. Am. Meteorol. Soc.* **78**, 21–34 (1997).
36. Trenberth, K. E. et al. Progress during TOGA in understanding and modeling global teleconnections associated with tropical sea surface temperatures. *J. Geophys. Res. Oceans* **103**, 14291–14324 (1998).
37. Deser, C. On the teleconnectivity of the 'Arctic Oscillation'. *Geophys. Res. Lett.* **27**, 779–782 (2000).
38. Alexander, M. A. et al. The Atmospheric Bridge: The Influence of ENSO Teleconnections on Air–Sea Interaction over the Global Oceans. *J Clim* **15**, 2205–2231 (2002).
39. Ashok, K., Behera, S. K., Rao, S. A., Weng, H. & Yamagata, T. El Niño Modoki and its possible teleconnection. *J. Geophys. Res. Oceans* **112**, (2007).
40. Cai, W., van Rensch, P., Cowan, T. & Hendon, H. H. Teleconnection pathways of ENSO and the IOD and the mechanisms for impacts on Australian rainfall. *J. Clim.* **24**, 3910–3923 (2011).
41. Cai, W. et al. Pantropical climate interactions. *Science* **363**, (2019).
42. Cai, W. et al. Climate impacts of the El Niño–Southern Oscillation on South America. *Nat. Rev. Earth Environ.* **1**, 215–231 (2020).
43. Li, X. et al. Tropical teleconnection impacts on Antarctic climate changes. *Nat. Rev. Earth Environ.* **2**, 680–698 (2021).
44. Hu, D. & Guan, Z. Relative effects of the greenhouse gases and stratospheric ozone increases on temperature and circulation in the stratosphere over the Arctic. *Remote Sens (Basel)* **14**, (2022).
45. Solomon, S., Garcia, R. R., Rowland, F. S. & Wuebbles, D. J. On the depletion of Antarctic ozone. *Nature* **321**, 755–758 (1986).
46. Son, S. W. et al. Impact of stratospheric ozone on Southern Hemisphere circulation change: a multimodel assessment. *J. Geophys. Res. Atmos.* **115**, (2010).
47. McLandress, C. et al. Separating the dynamical effects of climate change and ozone depletion. Part II: Southern Hemisphere troposphere. *J. Clim.* **24**, 1850–1868 (2011).
48. Previdi, M. & Polvani, L. M. Climate system response to stratospheric ozone depletion and recovery. *Q. J. Roy. Meteorol. Soc.* **140**, 2401–2419 (2014).
49. Fogt, R. L. & Marshall, G. J. The Southern Annular Mode: Variability, trends, and climate impacts across the Southern Hemisphere. *Wiley Interdisciplinary Rev.: Clim. Change* **11**, https://doi.org/10.1002/wcc.652 (2020).

50. Serreze, M. C. & Barry, R. G. Processes and impacts of Arctic amplification: a research synthesis. *Glob Planet Change* **77**, 85–96 (2011).
51. Döscher, R., Vihma, T. & Maksimovich, E. Recent advances in understanding the Arctic climate system state and change from a sea ice perspective: a review. *Atmos. Chem. Phys.* **14**, 13571–13600, https://doi.org/10.5194/acp-14-13571-2014 (2014).
52. Walsh, J. E. Intensified warming of the Arctic: causes and impacts on middle latitudes. *Glob. Planet Change* **117**, 52–63 (2014).
53. Petoukhov, V. & Semenov, V. A. A link between reduced Barents-Kara sea ice and cold winter extremes over northern continents. *J. Geophys. Res. Atmos.* **115**, (2010).
54. Overland, J. et al. The urgency of Arctic change. *Polar Sci.* **21**, 6–13 (2019).
55. Saji, N. H., Goswami, B. N., Vinayachandran, P. N. & Yamagata, T. A dipole mode in the tropical Indian Ocean. *Nature* **401**, 360–363 (1999).
56. Hendon, H. H. Indonesian Rainfall Variability: Impacts of ENSO and Local Air-Sea Interaction. *J. Climate* **16**, 1775–1790 (2003).
57. Yang, J., Liu, Q. & Liu, Z. Linking observations of the Asian monsoon to the Indian Ocean SST: Possible roles of Indian Ocean Basin mode and dipole mode. *J. Clim.* **23**, 5889–5902 (2010).
58. Lee, T. & McPhaden, M. J. Increasing intensity of El Niño in the central-equatorial Pacific. *Geophys. Res. Lett.* **37**, (2010).
59. Yeh, S. W. et al. ENSO atmospheric teleconnections and their response to greenhouse gas forcing. *Rev. Geophys.* **56**, 185–206 (2018).
60. Wang, L., Yu, J.-Y. & Paek, H. Enhanced biennial variability in the Pacific due to Atlantic capacitor effect. *Nat. Commun.* **8**, 14887 (2017).
61. Hoskins, B. J. & Karoly, D. J. The steady linear response of a spherical atmosphere to thermal and orographic forcing. *J. Atmos. Sci.* **38**, 1179–1196 (1981).
62. Horel, J. D. & Wallace, J. M. Planetary-scale atmospheric phenomena associated with the southern oscillation. *Mon. Weather Rev.* **109**, 813–829 (1981).
63. Karoly, D. J. Southern Hemisphere circulation features associated with El Niño-Southern oscillation events. *J. Clim.* **2**, 1239–1252 (1989).
64. Kidson, J. W. Principal modes of Southern Hemisphere low-frequency variability obtained from NCEP–NCAR reanalyses. *J Clim* **12**, 2808–2830 (1999).
65. Soulard, N., Lin, H. & Yu, B. The changing relationship between ENSO and its extratropical response patterns. *Sci. Rep.* **9**, (2019).
66. Carleton, A. M. Atmospheric teleconnections involving the Southern Ocean. *J. Geophys. Res. Oceans* **108**, (2003).
67. Thompson And, D. W. J. & Wallace, J. M. Annular Modes in the Extratropical Circulation. Part I: Month-to-Month Variability. *J. Climate*, **13**, 1000–1016 (2000).
68. Thompson, D. W. J., Wallace, J. M. & Hegerl, G. C. Annular Modes in the Extratropical Circulation. Part II: Trends. *J. Climate*, **13**, 1018–1036 (2000).
69. Lim, E. P., Hendon, H. H. & Rashid, H. Seasonal predictability of the southern annular mode due to its association with ENSO. *J. Clim.* **26**, 8037–8054 (2013).
70. Madden, R. A. & Julian, P. R. Detection of a 40–50 day oscillation in the zonal wind in the Tropical Pacific. *J. Atmos. Sci.* **28**, 702–708 (1971).
71. Henderson, S. A. & Maloney, E. D. The impact of the Madden-Julian oscillation on high-latitude winter blocking during El Niño-Southern Oscillation events. *J. Clim.* **31**, 5293–5318 (2018).
72. Lim, E. P. et al. Why Australia was not wet during spring 2020 despite La Niña. *Sci. Rep.* **11**, (2021).
73. Roxy, M. K. et al. Twofold expansion of the Indo-Pacific warm pool warps the MJO life cycle. *Nature* **575**, 647–651 (2019).
74. Henderson, S. A., Maloney, E. D. & Barnes, E. A. The influence of the Madden-Julian oscillation on Northern Hemisphere winter blocking. *J. Clim.* **29**, 4597–4616 (2016).
75. Watson, P. A. G., Weisheimer, A., Knight, J. R. & Palmer, T. N. The role of the tropical West Pacific in the extreme Northern Hemisphere winter of 2013/2014. *J. Geophys. Res.* **121**, 1698–1714 (2016).
76. Gillett, Z. E., Hendon, H. H., Arblaster, J. M. & Lim, E.-P. Tropical and extratropical influences on the variability of the Southern Hemisphere wintertime subtropical jet. *J. Clim.* **34**, 4009–4022 (2021).
77. Cleland, E. E., Chiariello, N. R., Loarie, S. R., Mooney, H. A. & Field, C. B. Diverse responses of phenology to global changes in a grassland ecosystem. *Proc. Natl Acad. Sci.* **103**, 13740–13744 (2006).
78. Hochman, A., Harpaz, T., Saaroni, H. & Alpert, P. The seasons' length in 21st century CMIP5 projections over the eastern Mediterranean. *Int. J. Climatol.* **38**, 2627–2637 (2018).
79. Juckes, M. N., James, I. N. & Blackburn, M. The influence of Antarctica on the momentum budget of the southern extratropics. *Q. J. Roy. Meteorol. Soc.* **120**, 1017–1044 (1994).
80. Held, I. M. & Schneider, T. The surface branch of the zonally averaged mass transport circulation in the troposphere. *J. Atmos. Sci.* **56**, 1688–1697 (1999).
81. Gong, D.-Y. & Ho, C.-H. The Siberian High and climate change over middle to high latitude Asia. *Theor. Appl. Climatol.* **72**, 1–9 (2002).
82. Dow, W. J., Maycock, A. C., Lofverstrom, M. & Smith, C. J. The effect of anthropogenic aerosols on the Aleutian Low. *J Clim* **34**, 1725–1741 (2021).
83. Smith, D. M. et al. Role of volcanic and anthropogenic aerosols in the recent global surface warming slowdown. *Nat. Clim. Chang.* **6**, 936–940 (2016).
84. Mantua, N. J., Hare, S. R., Zhang, Y., Wallace, J. M. & Francis, R. C. A Pacific interdecadal climate oscillation with impacts on Salmon Production*. *Bull. Am. Meteorol. Soc.* **78**, 1069–1080 (1997).
85. Gulev, S. K., Zolina, O. & Grigoriev, S. Extratropical cyclone variability in the Northern Hemisphere winter from the NCEP/NCAR reanalysis data. *Clim. Dyn.* **17**, 795–809 (2001).
86. Cohen, J. & Barlow, M. The NAO, the AO, and global warming: how closely related? *J. Clim.* **18**, 4498–4513 (2005).
87. Iles, C. & Hegerl, G. Role of the North Atlantic Oscillation in decadal temperature trends. *Environ. Res. Lett.* **12**, (2017).
88. Shaw, T. A. et al. Storm track processes and the opposing influences of climate change. *Nat. Geosci.* **9**, 656–664 (2016).
89. Winters, A. C., Keyser, D. & Bosart, L. F. The development of the North Pacific jet phase diagram as an objective tool to monitor the state and forecast skill of the upper-tropospheric flow pattern. *Weather Forecast* **34**, 199–219 (2019).
90. Sardeshmukh, P. D. & Hoskins, B. J. The generation of global rotational flow by steady idealized tropical divergence. *J. Atmos. Sci.* **45**, 1228–1251 (1988).
91. Fogt, R. L., Jones, J. M. & Renwick, J. Seasonal zonal asymmetries in the southern annular mode and their impact on regional temperature anomalies. *J. Clim.* **25**, 6253–6270 (2012).
92. Jones, J. M. et al. Assessing recent trends in high-latitude Southern Hemisphere surface climate. *Nat. Clim. Chang.* **6**, 917–926 (2016).
93. Kidston, J., Renwick, J. A. & McGregor, J. Hemispheric-scale seasonality of the southern annular mode and impacts on the climate of New Zealand. *J. Clim.* **22**, 4759–4770 (2009).
94. Ding, Q., Steig, E. J., Battisti, D. S. & Wallace, J. M. Influence of the tropics on the southern annular mode. *J. Clim.* **25**, 6330–6348 (2012).
95. Ding, Q., Steig, E. J., Battisti, D. S. & Küttel, M. Winter warming in West Antarctica caused by central tropical Pacific warming. *Nat. Geosci.* **4**, 398–403 (2011).
96. Clem, K. R. et al. Record warming at the South Pole during the past three decades. *Nat. Clim. Chang.* **10**, 762–770 (2020).
97. Ferreira, D., Marshall, J., Bitz, C. M., Solomon, S. & Plumb, A. Antarctic ocean and sea ice response to ozone depletion: a two-time-scale problem. *J. Clim.* **28**, 1206–1226 (2015).
98. Perlwitz, J. Tug of war on the jet stream. *Nat. Clim. Chang.* **1**, 29–31 (2011).
99. Hartmann, D. L. The Antarctic ozone hole and the pattern effect on climate sensitivity. *Proc. Natl Acad. Sci.* **119**, e2207889119 (2022).
100. Dong, Y., Armour, K. C., Battisti, D. S. & Blanchard-Wrigglesworth, E. Two-way teleconnections between the Southern Ocean and the Tropical Pacific via a dynamic feedback. *J. Clim.* **35**, 2667–2682 (2022).
101. Robinson, W. A. A baroclinic mechanism for the Eddy feedback on the zonal index. *J. Atmos. Sci.* **57**, 415–422 (2000).
102. Wills, R. C. J., Dong, Y., Proistosecu, C., Armour, K. C. & Battisti, D. S. Systematic climate model biases in the large-scale patterns of recent sea-surface temperature and sea-level pressure change. *Geophys. Res. Lett.* **49**, (2022).
103. Chemke, R., Ming, Y. & Yuval, J. The intensification of winter mid-latitude storm tracks in the Southern Hemisphere. *Nat. Clim. Chang.* https://doi.org/10.1038/s41558-022-01368-8 (2022).
104. Yamada, R. & Pauluis, O. Annular mode variability of the atmospheric meridional energy transport and circulation. *J. Atmos. Sci.* **72**, 2070–2089 (2015).
105. Dee, D. P. et al. The ERA-Interim reanalysis: Configuration and perform ance of the data assimilation system. *Q. J. Roy. Meteorol. Soc.* **137**, 553–597 (2011).
106. Hersbach, H. et al. The ERA5 global reanalysis. *Q. J.Roy. Meteorol. Soc.* **146**, 1999–2049 (2020).

Acknowledgements

The authors thank FengFei Song, Clemens Spensberger, an anonymous reviewer and editors for their comments on the submitted manuscript. We are also grateful to Andrew Dowdy and Matthew Wheeler for their feedback on the earlier version of the manuscript. P.H. thanks Mei Zhao for sharing her research ideas. This work has been supported by the Department of Energy, Environment, and Climate Action under Victorian Water and Climate Initiative. G.B., A.P. and P.H. were supported in part by the Australian government's National Environmental Science Program. We acknowledge the assistance of resources and services from the National Computational Infrastructure (NCI), supported by the Australian Government.

Author contributions

I.R. conceptualized the research, contributed to the analysis, and led writing of the manuscript. G.B. performed the analysis and helped conceptualize the research. C.L. conceptualizsed the research and calculated the isentropic stream function values. L.A. performed initial analysis. A.P. contributed to the analysis. P.H. contributed to the discussion of the results. All authors provided input to the draft and contributed to the writing of the final paper.

Competing interests

The authors declare no competing interests.

Additional information

Supplementary information The online version contains supplementary material available at https://doi.org/10.1038/s43247-023-00785-7.

Correspondence and requests for materials should be addressed to Irina Rudeva.

Peer review information *Communications Earth & Environment* thanks FengFei Song, Clemens Spensberger and the other, anonymous, reviewer(s) for their contribution to the peer review of this work. Primary Handling Editors: Min-Hui Lo, Clare Davis, Heike Langenberg.